Impedance study of membrane dehydration and compression in proton exchange membrane fuel cells

Jean-Marc Le Canut [1], Ruth Latham [2], Walter Mérida [3], David A. Harrington*

Institute for Integrated Energy Systems, University of Victoria, Victoria, British Columbia, Canada V8W 3P6

ABSTRACT

Electrochemical impedance spectroscopy (EIS) is used to measure drying and rehydration in proton exchange membrane fuel cells running under load. The hysteresis between forward and backward acquisition of polarization curves is shown to be largely due to changes in the membrane resistance. Drying tests are carried out with hydrogen and simulated reformate (hydrogen and carbon dioxide), and quasi-periodic drying and rehydration conditions are studied. The membrane hydration state is clearly linked to the high-frequency arc in the impedance spectrum, which increases in size for dry conditions indicating an increase in membrane resistance. Changes in impedance spectra as external compression is applied to the cell assembly show that EIS can separate membrane and interfacial effects, and that changes in membrane resistance dominate. Reasons for the presence of a capacitance in parallel with the membrane resistance are discussed.

© 2009 Elsevier B.V. All rights reserved.

1. Introduction

Proton exchange membrane fuel cells (PEMFC) appear to be a very promising technology, particularly for stationary power generation and for vehicles applications. Low operating temperatures and the use of a solid electrolyte give advantages of short start-up times, and the ability to operate in any orientation. A key issue is water management, which has a major impact on overall system power and efficiency. Single cell and stack performance may be adversely affected by the formation of liquid water in the gas diffusion layers or in the flow-field channels, by the dilution of the reactant gases by water vapor, or by dehydration of the polymer electrolyte membrane (PEM). Dehydration affects the membrane morphology and properties, by reducing the size of the ionic clusters, and the width of the interconnecting channels within the polymer's microstructure. The reduced protonic mobility leads to an increase in membrane resistance, and thus to an increase in power loss due to the ohmic heating associated with the ionic current through the membrane. Uneven heating can dry out the membrane in specific regions, leading locally to higher resistances

and therefore exacerbating the heating in those regions. Ultimately, this runaway process can completely remove water, raise the local temperature above the polymer's glass transition temperature and lead to irreversible degradation of the membrane. Severe degradation of this type can produce holes or voids in the membrane, resulting in a risk of fire or explosion from the direct mixing of hydrogen and oxygen [1–3].

Here we measure membrane properties and membrane drying in fuel cells under load using electrochemical impedance spectroscopy (EIS). EIS has been used to study many aspects and components of PEMFCs, including complete cells and stacks. Mérida et al. [4,5] give a large number of references to earlier work, and stress the utility of EIS for diagnostic purposes for fuel cells running under load. The experimental protocol used here is the same as in that work. The diagnostic utility of EIS on larger industrial-scale stacks was demonstrated by Le Canut et al. [6], where flooding, drying and catalyst poisoning faults were shown to be distinguishable by EIS. Commercial stacks have also recently been studied by Yuan et al. [7]. Here we focus less on the diagnostic implications, and on a more detailed study of the influence of drying and compression on the impedance spectra, particularly on the parts associated with the membrane. The membrane resistance is found to be in parallel with a capacitance whose nature is discussed. We discuss also the effect of cell compression on these quantities.

2. Experimental

The details of the cell assembly and the method for impedance measurement have been given previously [5]. Briefly, a Solartron

* Corresponding author. Tel.: +1 250 7217166; fax: +1 250 7217147.
 E-mail addresses: jean-marc.le-canut@utbm.fr (J.-M. Le Canut), RLatham@Tenneco.com (R. Latham), wmerida@interchange.ubc.ca (W. Mérida), dharr@uvic.ca (D.A. Harrington).
 [1] Present address: INEVA-CNRT, UTBM, rue Thierry Mieg, 90010 Belfort, France.
 [2] Present address: Tenneco Inc., Grass Lake, MI 48103, USA.
 [3] Present address: Clean Energy Research Centre, University of British Columbia, Vancouver, BC, Canada V6T 1Z4.

Frequency Response Analyser (FRA) generated an ac voltage that controlled the ac current through the fuel cell via a load bank (TDI-Dynaload MCL488). The ac current through the fuel cell was measured by converting it to a voltage with a shunt resistor in series with the fuel cell, and this voltage and the voltage across the fuel cell were fed to the two analyser channels of the FRA. Careful attention was paid to cable layout and connection issues. Specifically we used equal length coaxial cables to the differential inputs, which were twisted together and made 90° angles to the shunt, to which they were firmly connected with screw connectors. These precautions and the use of a shunt resistor external to the load bank enabled us to use an extended frequency range (0.5 Hz to 50 kHz), with the highest frequency being somewhat higher than the 20 kHz nominal frequency response of the load bank [5]. The use of the internal current measuring capability of the load bank, as used by Tang et al. [8], is simpler but restricts the frequency range (unless the frequency response of the current measuring circuit could be demonstrated to be much faster than the feedback electronics).

A Fuel Cell Test Station (Ballard Power Systems-ASA) provided conditioned fuel and oxidant streams. The main station delivered the fuel gas, the oxidant gas, nitrogen for conditioning of the cell assembly (bladder pressure), and deionized water at controlled temperature. The humidification station conditioned the reactants before they entered the fuel cell. The anodic or cathode compartments were separately supplied with dry or humid gas at controlled temperatures. Experiments were carried out at 207 kPa (gauge) for both the fuel (hydrogen or reformate mixture) and the oxidant (air).

A single-cell test rig allowed convenient assembly of a membrane electrode assembly (MEA) between two parallel graphite plates, each with a single serpentine channel. Two external temperature-controlled compartments permitted the MEA to be easily changed, and a bladder or a piston was used to control the pressure applied to the fuel cell. MEAs from different manufacturers were used as noted, all with a geometric area of 30 cm^2.

3. Results

3.1. Typical spectra and equivalent circuit

Fig. 1 shows a typical Nyquist plot and the circuit that fits most of the PEMFC data generated in our laboratory. At the highest frequencies measured, the impedance tends to the real axis at a resistance that is very small (ca. 20 mΩ cm^2). This is the resistance between the external current-carrying conductors and the active electrochemical surface, comprising the ohmic resistances of the graphite plates, carbon electrode/gas diffusion layers, carbon catalyst support particles and Pt catalyst particles themselves, and any contact resistances between and within these components. We refer to this as the contact resistance, R_c. A "high-frequency arc" shows as a semicircle between the highest frequencies and about 1 kHz. As discussed below, the diameter of this feature is consistent with the resistance that is calculated from the known geometry and conductivity of the Nafion membrane and is therefore assigned to the ionic membrane resistance, R_m. The capacitance associated with this is denoted C_m. Careful cable layout is required to avoid a high frequency inductive artifact that can suppress the high-frequency arc and lead to the impedance crossing below the real axis at a value approximating $R_c + R_m$.

At frequencies lower than about 1 kHz, a "mid-frequency" arc is observed that is attributed to electrochemical and mass transport features. This was modelled as a double-layer capacitance C_{dl} parallel to a series combination of a charge-transfer resistance R_{ct} (mostly attributed to the slow kinetics of oxygen reduction at the cathode) and a generalized finite-length-diffusion Warburg impedance ($Z_W = R_W \tanh(i\omega\tau)^p/(i\omega\tau)^p$ with $p \approx 1/2$). Under some
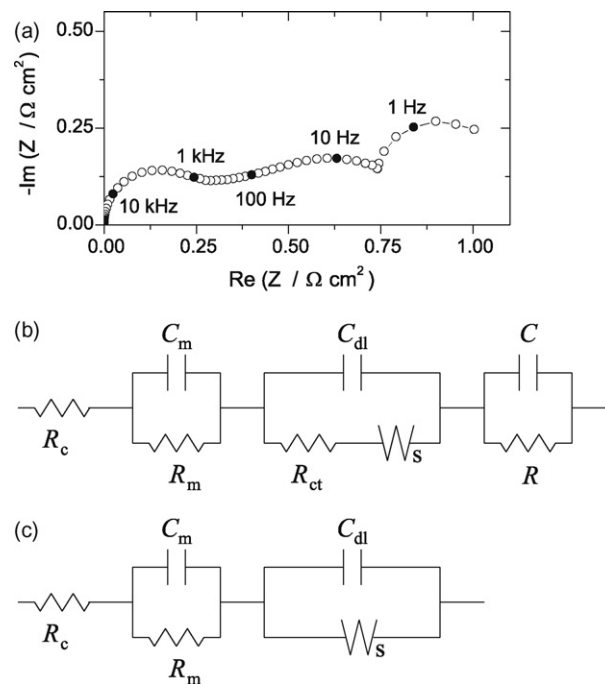

Fig. 1. Fuel cell impedance spectroscopy. (a) spectrum showing all typical features, (b) equivalent circuit, (c) simplified circuit used for fitting in this work.

conditions this mid-frequency feature appeared as two arcs and could not be modelled so simply. A third "low-frequency" arc was sometimes seen at lower frequencies, was modelled as a parallel RC combination, and may be due to the mass transport limitations at the anode [9,10].

3.2. Polarization dependence

Impedance spectra were measured at different points along the steady-state polarization curve. A true steady state can be difficult to reach because the cell produces heat over the course of the experiment, and because drying, flooding or other processes cause slow changes. We achieved quasi-steady state conditions with a cell voltage decay close to 1 mV between the beginning and the end of an impedance run. This should be sufficient for a stationary response and therefore valid impedance measurements. Nonetheless, hysteresis is observed between the polarization curves obtained in the direction of increasing current densities (the "direct" curve) and those obtained in the direction of decreasing current densities (the "reverse" curve), Fig. 2. The reverse curve shows better performance and its linear part is better defined. The difference in potential is as much as 80 mV in the low current density region. Such hysteresis has been seen before, e.g., [11].

The impedance spectra make clear the cause of the hysteresis. Fig. 3 (left) shows 3D plots of the spectra taken along the direct and reverse polarization curves. Three isofrequency lines at 1 kHz, 100 Hz and 1 Hz reveal the changes in the impedance with the current density. The low frequency limit of the impedance is the polarization resistance, i.e., the slope of the polarization curve. The slope is higher in the initial activation-controlled region and the final mass-transport controlled region, and smaller in the intermediate region controlled by the membrane resistance. The size of the impedances at the lowest frequencies and the 1 Hz isofrequency lines show the expected correlation with the slopes.

Only the high- and mid-frequency arcs are seen at low current densities. The mid-frequency arc is large at the lowest current density, then it decreases rapidly in size. The intermediate current densities show some evidence of the low frequency arc.
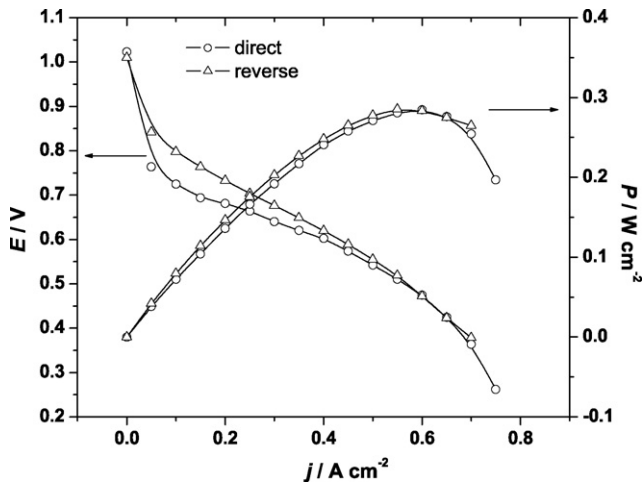
Fig. 2. Polarization curves. Cell potential and power density as a function of current density. The direct curve was acquired in the direction of increasing current densities and the reverse curve was acquired in the direction of decreasing current densities. MER Corp MEA (Nafion 115, anode loading 0.5 mg Pt cm^{-2}, cathode loading 1.0 mg Pt cm^{-2}), $T_{cell} = 50\,°C$, $T_{H_2} = T_{air} = 60\,°C$, $p_{H_2} = p_{air} = 207$ kPa (gauge), flow rates 0.75 standard L min^{-1} (air), 0.4 standard L min^{-1} (H$_2$).

Superposition of the overall diagrams (Fig. 3, right) reveals an unchanged high frequency arc in the case of the reverse curve, for all the current densities studied. On the other hand, this arc is higher at the initial low current densities for the direct curve. Since the diameter of this arc measures the membrane resistance, these results give a clear explanation of the hysteresis. At the lowest current densities on the direct curve, the membrane is not well hydrated, but moving to higher current densities increases the rate of water production and leads to greater hydration; a fully hydrated state is reached after about 0.4 A cm^{-2}. On the reverse curve however, the membrane is fully hydrated at the highest current density, and no significant change in membrane hydration is observed as the current density is reduced. This explanation was given before [11], but without experimental evidence.

To quantitate these effects, we simplified the circuit of Fig. 1b to that of Fig. 1c by omitting the elements C and R. This assumption is valid if we use a restricted frequency range for data fitting. Non-linear fitting was done using ZView software over the frequency range from 50 Hz to 50 kHz. Preliminary fitting showed that because R_{ct} was much smaller than R_W, it could not be reliably determined and so was omitted from the circuit for the fits shown here. For example, at 0.4 A cm^{-2} in the direct direction where the mid-frequency arc is noticeable, R_{ct} was $0.010 \pm 0.012\,\Omega$ cm^2 probably not significantly different from zero but in any case small compared to $R_W = 0.391 \pm 0.018\,\Omega$ cm^2. At the highest current densities it is certainly negligible. The dependence of the parameters on poten-
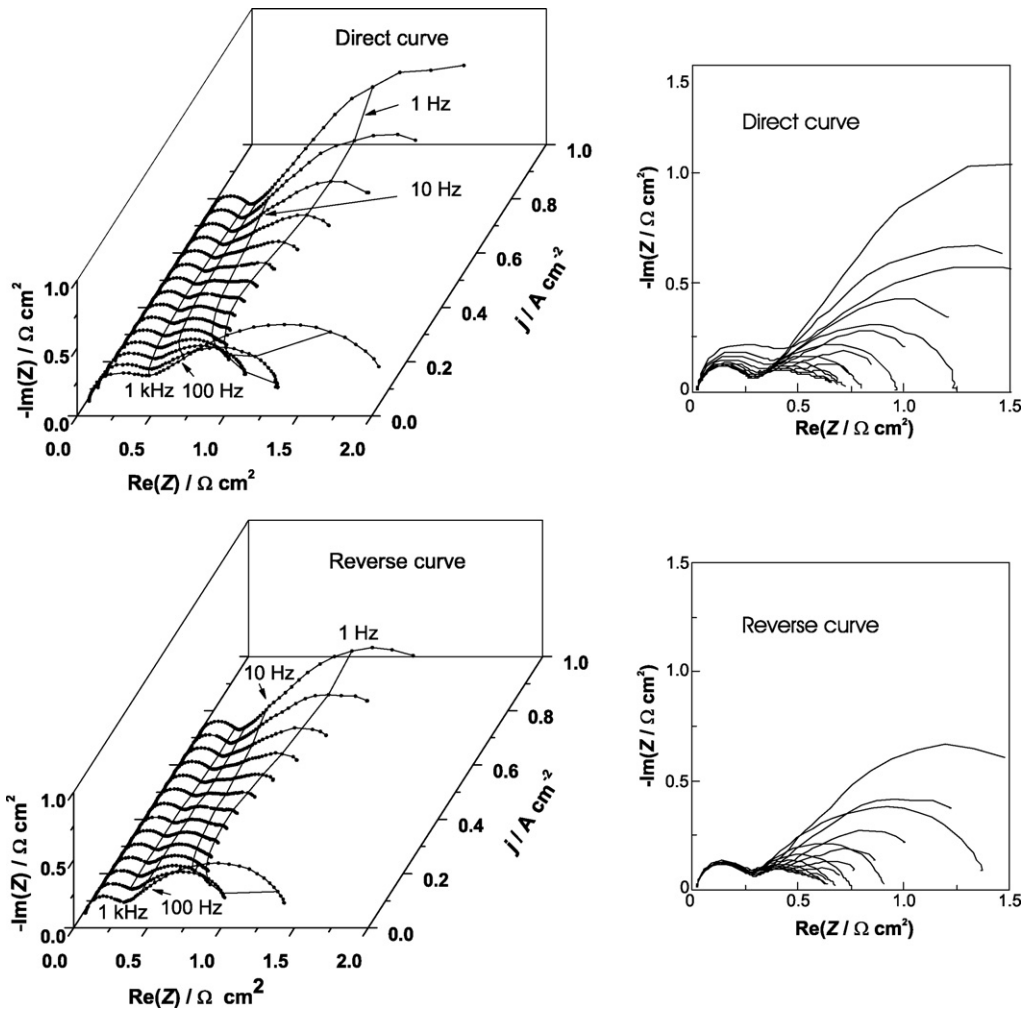

Fig. 3. Impedance data along the direct and reverse polarization curves of Fig. 2. Left: 3D plots showing the potential dependence of the spectra. Right: superimposed Nyquist plots show that the high-frequency semicircles are unchanging only for the reverse curve.
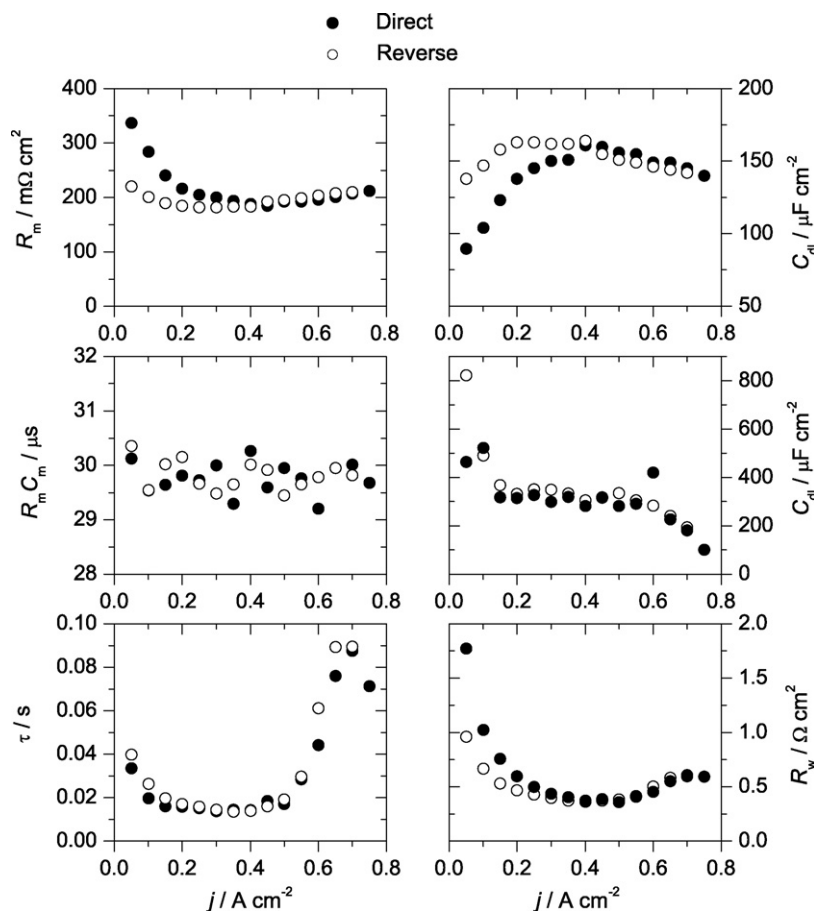
Fig. 4. Change in fitted equivalent circuit parameters with current density along the direct and reverse curves in Fig. 2.

tial (Fig. 4) shows quantitatively the change in electrochemical and transport parameters, as we well as the membrane resistance and capacitance and the contact resistance. Despite changes in both the membrane capacitance and resistance, the time constant R_mC_m is remarkably constant at $30 \pm 1\,\mu s$. As expected, the contact resistance R_c is potential independent ($21 \pm 2\,m\Omega\,cm^2$). The interfacial and mass-transport parameters C_{dl}, R_W and τ change singnifcantly; the Warburg exponent is 0.36 ± 0.08 (3σ), significantly less than the theoretical value of 1/2. All parameters are characterized by a plateau for current densities ranging from 0.1 to 0.5 A cm^{-2}.

Resistance has been correlated to hysteresis in polarization curves before [12,13]. Those workers measured the impedance at one frequency to determine resistance, and so were not able to measure the other parameters. They found more hysteresis in the resistance than we do here, but this is likely accounted for the fact that they collected data under faster potentiodynamic conditions.

3.3. Dehydration experiments

Insufficient humidification of the incoming gas streams leads to diminished cell potentials, and ultimately the membrane can dry out enough to be damaged. This drying process occurs gradually over a time frame of about 40 min in our experiments, and the time taken to acquire an impedance spectrum is such that the system is changing slowly during acquisition. This effect was minimized by restricting the frequency range to 1 Hz to 10 kHz, leading to quasi stable spectra in which the membrane properties at the higher frequencies are reliably determined, but the lowest frequency features may be distorted. A single cell was used, having an MER Corp. MEA with Nafion 115, anode Pt loading of 0.4 mg cm^{-2}, and cathode Pt

loading of 0.7 mg cm^{-2}. The cell was maintained at 60 °C and the fuel and air streams were humidified and maintained at 70 °C before switching to dry streams of the same compositions and temperatures. The drying process led to a decay of 200–300 mV in cell potential over about 40 min and was allowed to continue until the cell potential dropped below ca. 300 mV. Then the cell was rehydrated by switching back to the humidified fuel and air streams. Fig. 5 shows the drying at $j = 0.3$ A cm^{-2} with (a) pure hydrogen and (b) a reformate mixture (70% H$_2$, 24% CO$_2$, 6% N$_2$). These conditions are close to real working conditions for PEMFCs.

The drying test carried out with pure hydrogen was followed by cell rehydration. We observe that full recovery is not immediately achieved because the cell voltage after test (point *j*) is lower than the initial cell voltage (point *a*). This is similar to the cell voltage decay observed for the first 60 min after startup. The recovery transient was not recorded in the case of reformate.

The 3D impedance plots show that drying shifts the impedance points to the right, i.e., increases the impedance. (For clarity, the last two impedance spectra on the left in Fig. 5 are shifted by +15 min.) The isofrequency line at 500 Hz is affected by drying in the case of H$_2$ but not significantly in the case of the reformate mixture. Because the system is changing with time, fitting was done over a restricted frequency range of 1–5 kHz, using a simpler equivalent circuit (Fig. 1c without C_{dl} and the Warbug impedance). For both H$_2$ and reformate, the membrane resistance increases with drying, while capacitance decreases (Fig. 6).

The effect of the anode composition shows as a lower increase in the membrane resistance obtained with the reformate mixture (0.3–0.4 Ω cm^2) compared to H$_2$ (0.3–0.8 Ω cm^2). The reformate causes changes in the anode kinetic and/or anode mass transport,
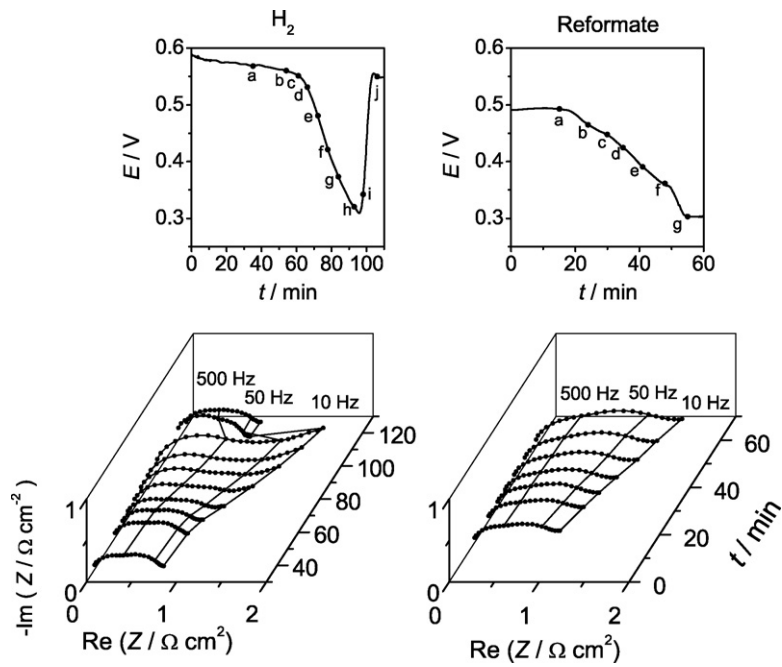
Fig. 5. Changes with time during drying at 0.3 A cm^{-2}. Top: cell voltage; bottom: impedance spectra; left: H$_2$ anode gas; right: reformate anode gas.

and shifts the impedance diagrams to the right. The membrane time constant changes only slightly with the drying effect and the values for H$_2$ and the reformate mixture are close. In a diagnostic situation, a simpler measurement such as the magnitude of the impedance at 500 Hz suffices to follow the drying trend (open circles), but values of the membrane resistance estimated by this method are not accurate. Details of diagnostic signatures such as this that also distinguish drying faults from other failure modes have been given previously [5,6].

Drying can also be caused by inappropriate working conditions. Fig. 7 shows the change in the cell voltage and the impedance

spectra when the cell temperature is higher than the inlet gas temperatures. In that case the partial pressure of the water vapor inside the fuel cell increases. This causes the product and input water to be removed more rapidly in the form of water vapor by the gas flow. This effect limits the humidification of the fuel cell, leading to drying conditions for the membrane. Experiments were carried out in a single cell (MEA: MER Corp., Nafion 115, Pt loading = 0.5 mg Pt cm^{-2} (anode), 1.0 mg Pt cm^{-2} (cathode)) at j = 0.4 A cm^{-2}. The gas temperatures were 70 °C, and the cell temperatures were at 80 °C (Fig. 7, left) or 90 °C (Fig. 7, right). With these particular sets of conditions, we have been able to get quasi-periodic phenomenon with slow
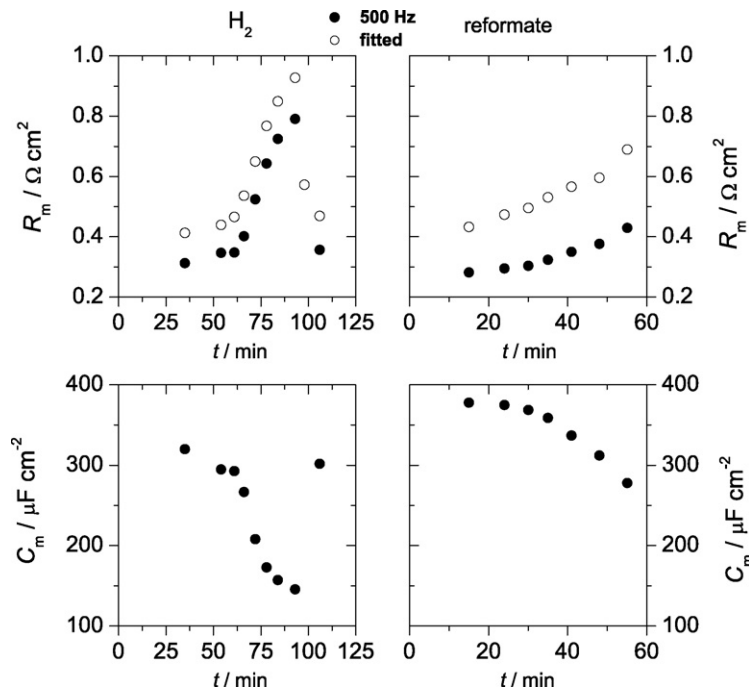

Fig. 6. Change in the membrane capacitance and resistance with time during drying. Left: H$_2$ anode gas; right: reformate anode gas. Solid circles are from fits of the spectra to the equivalent circuit model; open circles are estimates made from a single data point at 500 Hz (see text).
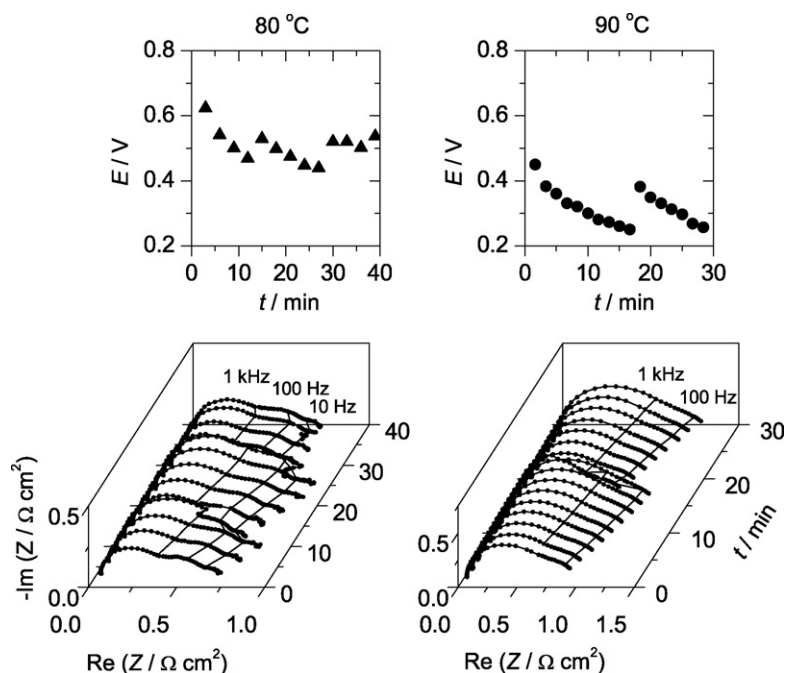
Fig. 7. Quasi-periodic drying. Top: cell voltages with time; bottom: corresponding impedance spectra. Left: $T_{cell} = 80\,°C$; right: $T_{cell} = 90\,°C$.

drying followed by rapid rehumidification. For both cell temperatures, there is a slow periodic variation of the fuel cell voltage, which decreases slowly for 10–15 min, and then recovers or partly recovers more rapidly in 1–2 min. Increasing the cell temperature results in higher drying conditions: the fuel cell voltage is lowered and the decay in potential is more pronounced.

Impedance experiments were recorded continuously in both cases (Fig. 7, bottom). Impedance data at 80 °C were obtained in the frequency range 0.5 Hz to 50 kHz. In that case, acquisition of each impedance diagram takes about 3 min, and the acquisition is not stationary since several dozen or more than a hundred mV can be lost or gained in a run. Impedance data obtained at 90 °C were collected over a more restricted range (50 Hz to 50 kHz) permitting a faster acquisition for each impedance diagram.

The transition event between a low voltage value and the recovered voltage can be clearly seen on the impedance diagrams. Fig. 7 bottom left shows an increase in the three isofrequency lines with the decrease in the cell voltage. Each time the cell voltage increases abruptly (at 13 or 27 min), the shape of the impedance diagram shows a discontinuity between the high frequency and the low frequency arcs. The high frequency impedance after this event is reduced and then the periodic process repeats. The shapes of the middle and the low frequency arcs do not change, except when an abrupt voltage event takes place during their acquisition. This is a good indication that the drying process affects mainly the membrane and much less the electrochemical and mass transport activities. For the driest condition, the change in the impedance plot with the time is close to the previous results (Fig. 5); the high frequency arc increases as the potential decreases and reduces suddenly when the potential increases again (Fig. 7, bottom right). The membrane resistance and capacitance were extracted as before. Fig. 8 shows the change in these parameters with time. These changes agree well with the changes in fuel cell voltage under drying conditions. The membrane resistance increases as the membrane dries and falls when the membrane is rehumidified.

Similar fluctuating or periodic behavior has been seen before by Atkins et al. [14], albeit at constant voltage conditions and on a slower timescale. They also found that resistance (as measured with

a current interrupt method) increased as performance decreased. Drying leads to increased resistance, which leads to higher ohmic heating and further drying. Atkins et al. suggested that the rehydration occurs becasue reduced electroosmotic drag reduces drying at the anode, it could also occur because liquid water accumulated in the cathode gas diffusion layer moves into the membrane. Benziger et al. [15] observed slower oscillations under constant external resistance conditions. These were explained [16,17] in terms of switching between states with uniform current density and states with localized fully hydrated pathways, the transition being mediated by lateral diffusion of water. This mechanism was also used to account for hysteresis in polarization curves.

3.4. Compression dependence

The effects of the compression of the cell assembly and of the type of gas diffusion layer on a single PEMFC have already been studied by Lee et al. [18] using steady state polarization measurements. Depending on the gas-diffusion-layer material, an optimal bolt torque was sometimes observed, with lower or higher assembly pressures giving reduced current density at a given voltage. We carried out experiments on a single cell test rig by varying the pressure applied to a piston compressing the fuel cell test assembly. The MEA studied was a proprietary design with a Nafion 117 membrane ($l = 170\,\mu m$), a catalyst layer and a gas diffusion layer made of Toray carbon fiber paper ($250\,\mu m$). The Pt catalyst loadings were $0.6\,mg\,cm^{-2}$ for the anode and $4.0\,mg\,cm^{-2}$ for the cathode.

The frequency response shows mainly two arcs and also a small inductive loop at the lowest frequencies (Fig. 9). This inductive feature, which we do not analyze further, has been attributed to peroxide production [19] or to drying effects [9,20], but we have also seen similar features that were artifacts [4]. The high frequency semicircle decreases as the pressure of the cell assembly is increased. At this low current density, the polarization resistance at the highest pressure is one third of the value obtained at low pressure. There is no change in the high resistance value (Fig. 9, inset), which is the residual contact resistance. These data were fitted using the equivalent circuit of Fig. 1c. The effect of compression on the membrane parameters vs the interfacial and
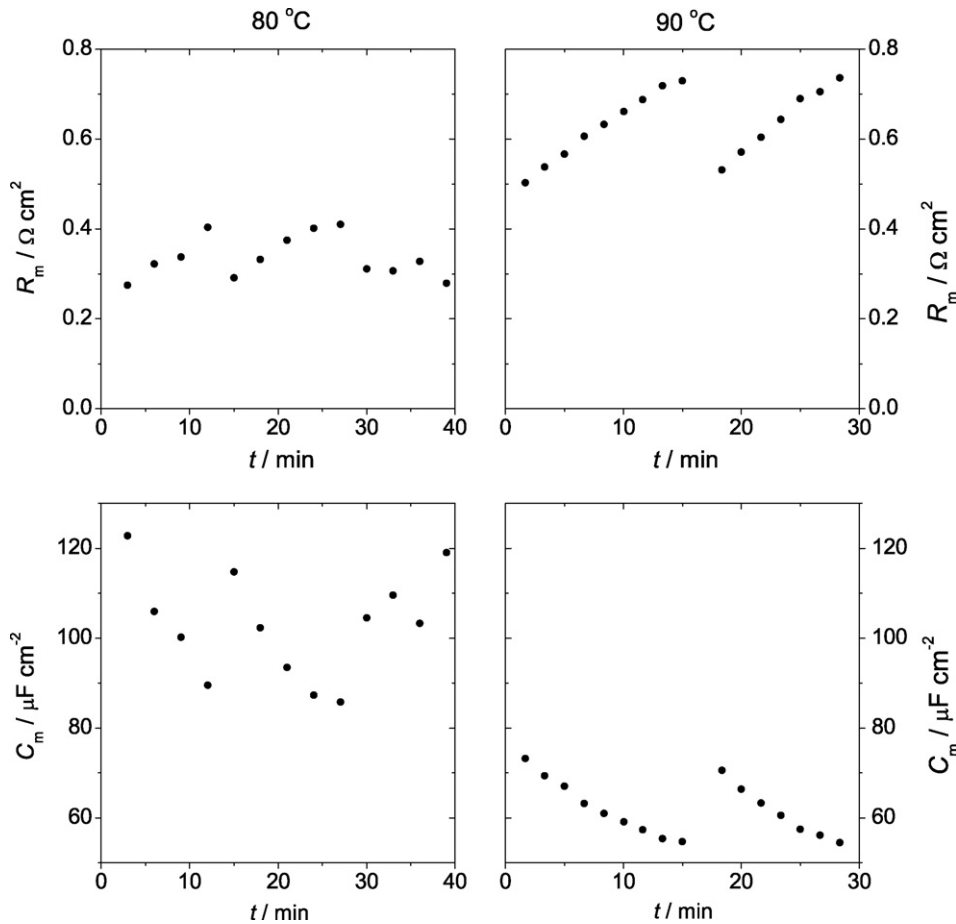
Fig. 8. Changes in membrane resistance and capacitance with time for the data of Fig. 7.
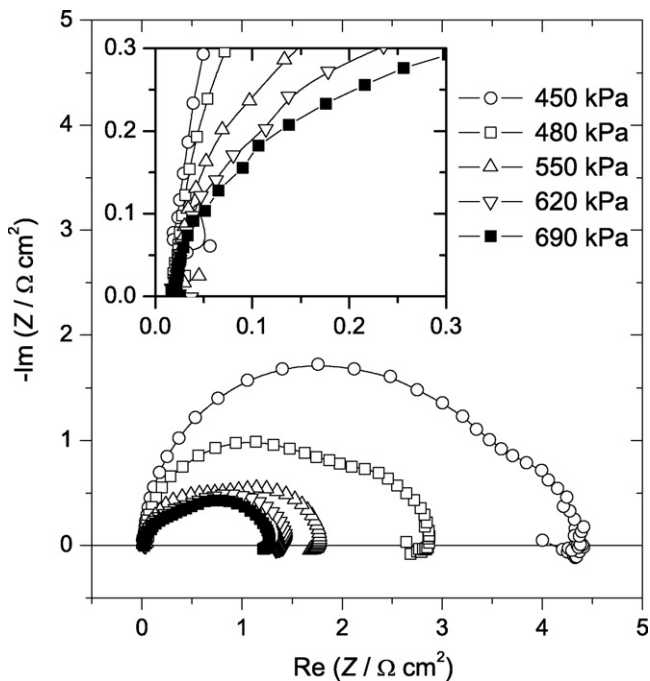

Fig. 9. Effect of the fuel cell test assembly pressure on the impedance diagrams. Ballard MEA; $T_{cell} = 70\,°C$, $j = 0.1\,A\,cm^{-2}$.

mass transport parameters is nicely summarized by displaying their contributions separately in Fig. 10. Part (a) of this figure shows the impedance of the leftmost part of the equivalent circuit, i.e., the parallel combination of R_m and C_m simulated using the fitted values of R_m and C_m; part (b) shows the rightmost part of the equivalent circuit with C_{dl} in parallel with the Warburg element. It is immediately evident that the membrane is most affected by the pressure, with the membrane resistance decreasing dramatically with pressure, which leads to a performance increase. The diffusion impedance decreases also, though the relative change is much smaller, and also leads to a performance increase. An optimum compression is not seen here, and this is consistent with the results of Lee et al. [18] for Toray-paper-based MEAs at lower current densities.

3.5. Active surface area and capacitance measurements

To interpret the measured capacitors, it is helpful to have an estimate of the active surface of the catalyst. We performed two-electrode cyclic voltammetry measurements on a selected MEA (E-Tek, Nafion 115, 450 μm ELAT/SS carbon cloth GDL, Pt loadings 0.4 mg Pt cm^{-2} (anode) and 2.0 mg Pt cm^{-2} (cathode)). The flow field on the cathode side of the MEA was filled with water and a slow flow of hydrogen was used on the anode side, making the anode a dynamic hydrogen reference electrode (DHE). The potential of the cathode was scanned, at 10 mV s^{-1} from +0.8 V vs DHE down to close to 0 V vs DHE. Integration of the hydrogen desorption peaks at 0.05–0.3 V (after baseline subtraction of the double-layer charging current) gave an active area of 345 cm^2 per cm^2 of MEA area, assuming the charge for an ideal flat surface is 210 μC cm^{-2}
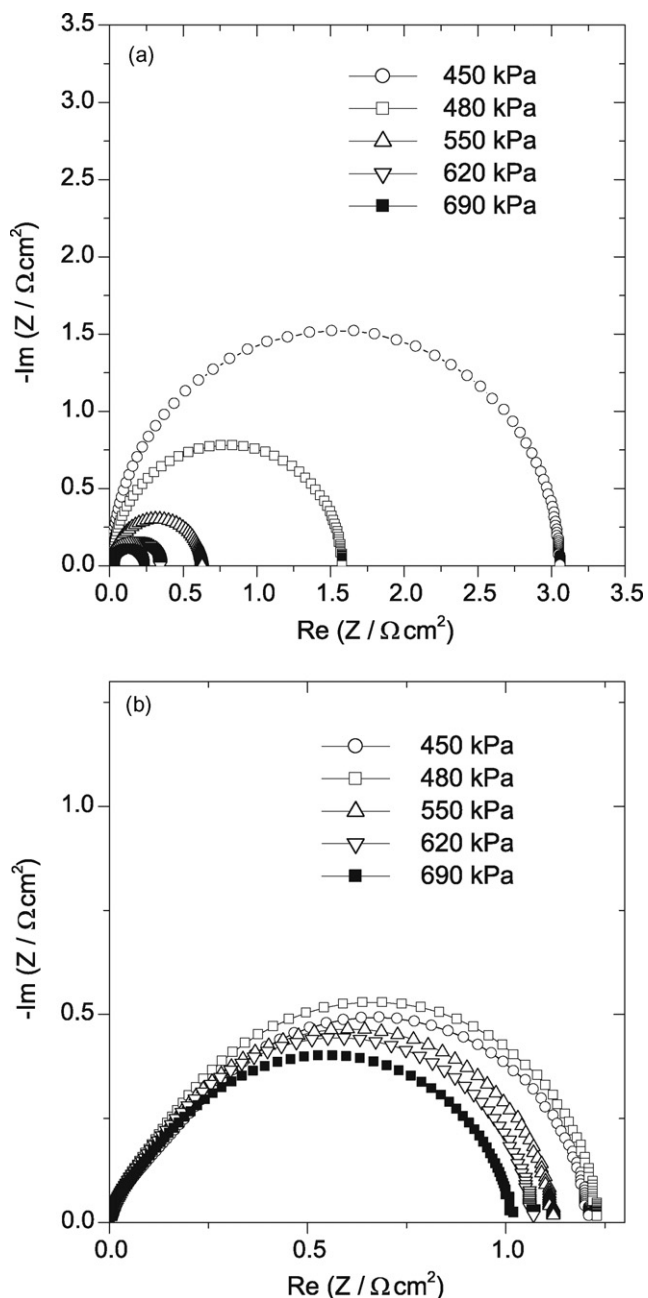
Fig. 10. Simulated impedance spectra from compression experiments using fitted parameters. (a) Membrane part of equivalent circuit (R_m and C_m in parallel), (b) interfacial part (C_m and Z_W in parallel).

This corresponds to 17 m^2 per gram of Pt. These values are similar to published results on comparable MEAs (120 cm^2 cm^{-2}, 13.3 m^2 g^{-1} [21]; 200 cm^2 cm^{-2}, 14 m^2 g^{-1} [22]; 14–115 m^2 g^{-1} (literature and measured values in [23]); 11–134 cm^2 cm^{-2} [24]).

The double layer capacitance was measured as the current in the "double-layer region" (0.4–0.6 V vs RHE) divided by the sweep rate, giving 0.13 F cm^{-2} (geometric area basis) or 375 μF cm^{-2} (active area basis). Classical values for smooth platinum are around 20 μF cm^{-2}, and the larger experimental value is probably an indication of the contribution of the carbon support in the catalyst and GDL. This is seen visually in the voltammogram as a larger baseline current relative to the hydrogen adsorption/desorption peak heights compared to smooth Pt voltammograms.

Table 1
Calculated membrane resistivities, conductivities and permittivities.

Experiment	σ (mS cm^{-1})	ρ (Ω cm)	ε_r
Compression 550 kPa, Fig. 9	28	36	1×10^7
Compression 620 kPa, Fig. 9	52	19	2.2×10^7
Polarization curves, Fig. 2	63	16	2.1×10^7
Drying, H$_2$ anode, Fig. 7	42	24	4.2×10^7
Drying, reformate anode, Fig. 7	45	22	5.4×10^7

4. Discussion

4.1. High-frequency semicircle

Typically, the high frequency semicircle above 1 kHz appears in our experiments on single cells, 4-cell stacks, and industrial scale stacks. To observe it requires care in cable layout and attention to good electrical contacts as described in Section 2; without these an inductive artifact replaces it and the impedance above about 1 kHz goes below the real axis on a Nyquist plot. This inductive feature is well known to be associated with cabling artifacts in laboratory-scale electrochemistry, and has frequently been seen also in fuel cell studies. Nonetheless, in studies of related systems where care is taken to remove the inductive artifact, high frequency semicircles similar to ours have been observed before [25–28,31–34,39], and in one case, both the inductive artifact and the semicircle was seen [7]. In most cases, as here, the semicircle is relatively independent of potential, and on this basis the diameter of the semicircle has been attributed to the membrane resistance. This interpretation is supported by the data here: drying leads to an increase in the diameter and in the membrane resistance because the membrane must be hydrated for proper proton conductivity. Drying also affects the electrochemistry and mass transport as indicated by the simultaneous effects in the lower-frequency parts of the spectra. On the other hand, cathode flooding affects largely the electrochemistry and mass transport and not the membrane: in that case the high-frequency semicircle is unaffected [5]. More significantly, the diameter of the semicircle has the value expected for the known resistivity and geometry of the membrane. Table 1 shows the resistivities of the membranes used here, calculated from Eq. (1) assuming a rectangular slab with the nominal Nafion thickness, d. (The geometric area is already included in R_m and C_m since they are expressed in units of Ω cm^2 and F cm^{-2} respectively.)

$$\rho = \frac{R_m}{d} = \frac{1}{\sigma} \tag{1}$$

These conductivity values agree well with those in the literature [25,35–40], though there is a large spread due to the variety of conditions and measurement methods used. Nonetheless, it is clear that the high-frequency intercept of the high-frequency semicircle (e.g., Fig. 9, inset) corresponds to a resistance value that is much too small to be the membrane resistance, and so we conclude that the membrane resistance is reasonably measured by the diameter of the semicircle.

The observation of a semicircle associated with the membrane suggests that the capacitance in parallel with the membrane resistance is also associated with the membrane. We note first that its value is much smaller than the double-layer capacitances discussed in the previous section, and so we assume that it does not originate from the double layer. If we treat it as a geometric capacitance, i.e., a parallel plate capacitor with the Nafion as a dielectric and take the thickness of the dielectric as the nominal membrane thickness, then we calculate from Eq. (2) the apparent dielectric constants in the last column of Table 1.

$$\varepsilon_r = \frac{C_m d}{\varepsilon_0} \tag{2}$$

The value of this capacitance has not always been extracted from impedance data, in some cases because the semicircle was more distorted than here, e.g., merged with the lower frequency arc [32], linked to the lower-frequency arc by an inductive loop [7] or flattened. Even when the interpretation has been as a geometric capacitance, the value of the capacitance or dielectric constant has usually not been commented on, e.g., [34]. We therefore consider the possible interpretations in more detail.

The very high dielectric constants seem to argue against a geometric capacitance, since typical bulk materials have dielectric constants less than 100. Nafion, having free mobile charges is not a typical material, however, and other workers have reported high dielectric constants for Nafion (measured outside of a fuel cell). Mauritz and Fu [41] have found high dielectric constants for Nafion, in the range of 10^2–10^5 and associated this with ion motion. However, even on pure materials, measurement artifacts are possible and have been discussed by several authors [42–44]. In the case of Nafion, Cahan et al.'s definitive work [44] shows that Nafion itself is purely resistive up to 100 kHz.

There is a miscellany of other explanations for high frequency semicircles, typically depending on the heterogeneous nature of the Nafion or the microstructure of the MEA: thin regions of intergrain or intercluster contact [25], a mixed geometric/double layer capacitance [27], a geometric capacitance including effects from the catalyst layer and the GDL [28], and other explanations invoking distributed processes associated with the catalyst layer or GDL or their contact with the membrane [26,29–32]. Not all of these are for semicircles with a diameter corresponding to the membrane resistance, as we have here, and most of them are suggestions with no theoretical support. It is known that suspended colloidal particles in an electrolyte can increase its effective dielectric constant by several orders of magnitude [45]. Catalyst particles that are electrically disconnected from the electrode would increase the dielectric constant within the catalyst layer by this mechanism. The higher-capacitance catalyst layer region would be in series with the lower-capacitance bulk membrane region and the overall capacitance would be dominated by the bulk membrane, so it is difficult to imagine that such effects could lead to dielectric constants as high as observed here.

We turn our attention to the possibility of artifacts caused by the measurement process itself. The high frequency arc appears more often in literature results for large-area, high-current cells. These systems have very low impedances, and one may expect measurement difficulties when the impedance of the object is comparable or smaller than contact and cable impedances. The shunt resistor ($R_s = 1$ mΩ) is deliberately small compared to the fuel cell impedance, to allow optimum operation of the load bank feedback control loop. Therefore we focused on the shunt and current measurement as the most likely source of artifacts. Measurement of the shunt impedance using the identical measurement setup showed that there was some frequency dispersion above a few kHz, that could be modelled as a series RC combination ($R_x = 9$ mΩ; $C_x = 2$ mF) in parallel with the shunt resistor itself. Whether this is due to the shunt itself or to cabling effects is not clear, but it means that the impedance calculated as $\widetilde{V}/(\widetilde{V}_s/R_s)$, where $\widetilde{V}$ and $\widetilde{V}_s$ are the ac voltage phasors measured on the voltage and current channels of the FRA, should really be $\widetilde{V}/(\widetilde{V}_s/Z_s)$ where Z_s includes the RC combination. Applying the correction factor R_s/Z_s gave only small changes to the spectra and parameters, did not significantly affect the fit quality, and therefore is not responsible for the existance or magnitude of the C_m. Although the Z_s correction was measured for the shunt (and may include cabling effects from both voltage and current measurment channels), one may speculate that the voltage measurement channel could require a similar correction, which might result in the series R_xC_x combination appearing in parallel across the fuel cell impedance. This correction gives small distortions in the spectra, but also cannot account for the presence of C_m. Another possibility is to note that since the R_mC_m time constant is the highest one measured, a similar semicircle could result from a circuit in which C_m was moved to be in parallel with all elements except R_c. This could lead to an interpretation of C_m that was unrelated to the membrane. It gave similar parameter values, except that C_{dl} was poorly determined. Since the fit was worsened by this procedure, we did not pursue it further.

We found that careful cable layout was required to get reproducible high-frequency semicircles, namely equal length coaxial cables to the differential inputs, twisted together, making 90° angles to the shunt and fixed firmly with screw connections. Once these precautions were taken, extending the cable lengths for the voltage or current measuring channels by a factor of three made no significant changes in the spectrum, and therefore we believe that cabling artifacts have been minimized. Although the systems are not directly comparable, it is notable that other measuring equipment also shows the high frequency semicircle (Gamry [6], Fuelcon [7]). These considerations cannot of course rule out that a common artifact exists for many measuring systems, but C_m does appear to be a robust feature of the spectra. From a practical point of view, using high enough frequencies to see the semicircle and then fitting to R_m and C_m allows for a more accurate determination of R_m than would be possible if only measuring below 1 kHz.

5. Conclusions

In this paper the increase in PEMFC membrane resistance with drying conditions was identified by EIS experiments and interpreted by means of models based on equivalent electrical circuits. Fuel cell drying causes an increase in membrane resistance. This can be identified as an increase in the size of the high frequency feature in fuel cell impedance diagrams. As fuel cell drying progresses and the cell voltage decreases, the feature becomes larger. The change in membrane resistance due to drying can be shown through fitting the data with an equivalent circuit model. The hysteresis observed between forwards and backwards acquisition of polarization curves has been shown, through impedance, to be due to the initial drying conditios for the membrane. Drying tests performed with pure hydrogen and a reformate mixture are characterized by an increase in the membrane resistance extracted after fitting the impedance data, which is much more pronounced in the case of pure hydrogen.

Membrane drying was found to be cyclic under specific conditions, i.e., when the amount of water produced at the cathode creates a sufficiently high concentration gradient such that water formed at the cathode diffusion layer is rapidly absorbed by the dried membrane. This was clearly revealed by the membrane resistance and membrane capacitance changes with time.

A study of progressive compression of the MEA assembly while the PEMFC was running showed a strong dependence of the membrane parameters with the compressive force applied to the fuel cell test assembly. EIS together with the equivalent circuit modelling revealed that the main contribution to the decrease in fuel cell impedance when the compression was increased was the membrane resistance.

The origin of the high frequency semicircles observed in all our experiments has been discussed in detail. The diameter corresponds to membrane resistance; membrane conductivities determined from it were similar to values experimentally found in the literature. The parallel capacitance measured corresponds to apparently high dielectric constant values that are discussed with respect to different literature interpretations and also to the possible occurrence of measurement artifacts. Careful attention to cable layout is crucial to get meaningful impedance results without an inductive artifact, but the capacitance remains and appears to be a robust feature of large-area fuel cells.

Acknowledgements

References

[1] D.P. Wilkinson, H.H. Voss, K. Prater, J. Power Sources 49 (1994) 117.
[2] J. Larminie, A. Dicks, Fuel Cell Systems Explained, John Wiley & Sons, Toronto, 2000.
[3] P. Costamagna, Chem. Eng. Sci. 56 (2001) 323.
[4] W.R. Mérida-Donis, Diagnosis of PEMFC failures via electrochemical impedance spectroscopy, Ph.D. thesis, University of Victoria, Canada, 2002.
[5] W. Mérida, D.A. Harrington, J.M. Le Canut, G. McLean, J. Power Sources 161 (2006) 264.
[6] J.-M. Le Canut, R.M. Abouatallah, D.A. Harrington, J. Electrochem. Soc. 153 (2006) A857.
[7] X. Yuan, J.C. Suna, M. Blanco, H. Wang, J. Zhang, D.P. Wilkinson, J. Power Sources 161 (2006) 920.
[8] Y. Tang, J. Zhang, C. Song, H. Liu, J. Zhang, H. Wang, S. Mackinnon, T. Peckham, J. Li, S. McDermid, P. Kozak, J. Electrochem. Soc. 153 (2006) A2036.
[9] I.A. Schneider, H. Kuhn, A. Wokaun, G.G. Scherer, J. Electrochem. Soc. 152 (2005) A2092.
[10] H. Kuhn, B. Andreaus, A. Wokauna, G.G. Scherer, Electrochim. Acta 51 (2006) 1622.
[11] J. Hamelin, K. Agbossou, A. Laperrière, F. Laurencelle, T.K. Bose, Int. J. Hydrogen Energy 26 (2001) 625.
[12] C. Ziegler, H.M. Yu, J.O. Schumacher, J. Electrochem. Soc. 152 (2005) A1555.
[13] H. Yu, C. Ziegler, J. Electrochem. Soc. 153 (2006) A570.
[14] J.R. Atkins, S.C. Savett, S.E. Creager, J. Power Sources 128 (2004) 201.
[15] J. Benziger, E. Chia, J.F. Moxley, I.G. Kevrekidis, Chem. Eng. Sci. 60 (2005) 1743.
[16] I. Nazarov, K. Promislow, Chem. Eng. Sci. 61 (2006) 3198.
[17] J.B. Benziger, E.-S. Chia, Y. De Decker, I.G. Kevrekidis, J. Phys. Chem. C 111 (2007) 2330.
[18] W.-K. Lee, C.-H. Ho, J.W. Van Zee, M. Murthy, J. Power Sources 84 (1999) 45.
[19] S.K. Roy, M.E. Orazem, B. Tribollet, J. Electrochem. Soc. 154 (2007) B1378.
[20] I.A. Schneider, M.H. Bayer, A. Wokaun, G.G. Scherer, J. Electrochem. Soc. 155 (2008) B783.
[21] M.C. Lefebvre, Z. Qi, P.G. Pickup, J. Electrochem. Soc. 146 (1999) 2054.
[22] M. Ciureanu, H. Wang, J. Electrochem. Soc. 146 (1999) 4031.
[23] A. Pozio, M. De Francesco, A. Cemni, F. Cardellini, L. Giorgi, J. Power Sources 105 (2002) 13.
[24] S.J. Lee, S. Mukerjee, J. McBreen, Y.W. Rho, Y.T. Kho, T.H. Lee, Electrochim. Acta 43 (1998) 3693.
[25] A. Parthasarathy, B. Davé, S. Srinivasan, A.J. Appleby, C.R. Martin, J. Electrochem. Soc. 139 (1992) 1634.
[26] S. Ahn, B.J. Tatarchuk, J. Electrochem. Soc. 142 (1995) 4169.
[27] J.T. Mueller, P.M. Urban, J. Power Sources 75 (1998) 139.
[28] V.A. Paganin, C.L.F. Oliveira, E.A. Ticianelli, T.E. Springer, E.R. Gonzalez, Electrochim. Acta 43 (1998) 3761.
[29] A. Fischer, J. Jindra, H. Wendt, J. Appl. Electrochem. 28 (1998) 277.
[30] O. Antoine, Y. Bultel, R. Durand, J. Electroanal. Chem. 499 (2001) 85.
[31] T.J.P. Freire, E.R. Gonzalez, J. Electroanal. Chem. 503 (2001) 57.
[32] T. Romero-Castañón, L.G. Arriaga, U. Cano-Castillo, J. Power Sources 118 (2003) 179.
[33] F. Liu, B. Yi, D. Xing, J. Yu, Z. Hou, Y. Fu, J. Power Sources 124 (2003) 81.
[34] P. Kurzweil, H.-J. Fischle, J. Power Sources 127 (2004) 331.
[35] P.D. Beattie, F.P. Orfino, V.I. Basura, K. Zychowska, J.F. Ding, C. Chuy, J. Schmeisser, S. Holdcroft, J. Electroanal. Chem. 503 (2001) 45.
[36] S.J. Paddison, D.W. Reagor, T.A. Zawodzinski Jr., J. Electroanal. Chem. 459 (1998) 91.
[37] C.L. Gardner, A.V. Anantaraman, J. Electroanal. Chem. 449 (1998) 209.
[38] F.N. Buchi, G.G. Scherer, J. Electroanal. Chem. 404 (1996) 37.
[39] M.C. Wintersgill, J.J. Fontanella, Electrochim. Acta 43 (1998) 1533.
[40] J.J. Sumner, S.E. Creager, J.J. Ma, D.D. DesMarteau, J. Electrochem. Soc. 145 (1998) 107.
[41] K. Mauritz, R.-M. Fu, Macromolecules 21 (1988) 1324.
[42] J.J. Fontanella, M.G. McLin, M.C. Wintersgill, Solid State Ionics 66 (1993) 1.
[43] G. Hsieh, S.J. Ford, T.O. Mason, L.R. Pederson, Solid State Ionics 100 (1997) 297.
[44] B.D. Cahan, J.S. Wainright, J. Electrochem. Soc. 140 (1993) L185.
[45] G. Schwarz, J. Phys. Chem. 66 (1962) 2626.